A New Dynamical Subgrid Model for the Planetary Surface Layer. Part I: The Model and A Priori Tests

BERENGERE DUBRULLE

SAp/DAPNIA/DSM/CEA, Gif sur Yvette, and CNRS, Observatoire Midi-Pyrénées, Toulouse, France, and NCAR, Boulder, Colorado

JEAN-PHILIPPE LAVAL

SAp/DAPNIA/DSM/CEA, Gif sur Yvette, France, and NCAR, Boulder, Colorado

PETER P. SULLIVAN

NCAR, Boulder, Colorado

JOSEPH WERNE

Colorado Research Associates Division, Northwest Research Associates Inc., Boulder, Colorado

(Manuscript received 20 September 1999, in final form 26 January 2001)

ABSTRACT

A new dynamical subgrid model for turbulent flow in the surface layer of the planetary boundary layer is presented. In this formulation, the flow is decomposed into small (subgrid) and large (resolved) scales in the spirit of large-eddy simulation. The subgrid model, however, is derived directly from the governing equations and involves no adjustable parameters. The evolution of the small scales is not postulated, but computed as a function of the large scales using a semiclassical method extending rapid distortion theory to account for the intermittency of the small scales. At the same time, feedback from the small scales to the large scales can also be computed via the corresponding subgrid stresses. The model can be generalized to include other physical effects, and thus could potentially be used to estimate momentum and temperature fluxes in complex systems like the planetary boundary layer, which impacts larger-scale models. A priori tests using 3D large-eddy and direct simulations of unstable, neutral, and stable flows support the assumptions in the model.

1. Introduction

The planetary surface layer (PSL) is the thin, lowest part of the atmospheric boundary layer. Despite its relatively small vertical extent (approximately 10% of the total boundary layer depth), the PSL is crucially important since it facilitates the exchange of momentum, heat, and scalar fluxes between land and ocean surfaces and the overlying atmosphere. Like many geophysical flows, the PSL is turbulent, and its computation by direct numerical simulation appears impossible because of the large Reynolds number involved. Presently, we can afford to simulate only the largest motions subject to a parameterization of the small scales using large-eddy simulation (LES) (e.g., Moeng and Sullivan 1994) or adopt an ensemble closure approach for all turbulence scales (Mellor 1973; Mellor and Yamada 1974). Both approaches involve adjustable constants, which cannot be derived from first principles and require calibration based on real data; surface similarity theory (e.g., Wyngaard 1992) is used in both types of modeling. The modeling constants are not necessarily universal (less so in LES) and frequently need to be varied according to the physical situation and stability properties of the surface layer.

This problem can be traced to parameterizations that are not directly derived from the equations, but rather postulated on purely phenomenological or dimensional grounds. The same problem exists in all subgrid-scale models used in high–Reynolds number LES [see Meneveau and Katz (2000) for a recent review]. A modeling difficulty with high–Reynolds flows, like the PSL, is the strong intermittency of the small-scale turbulence. In a stably stratified PSL, stratification inhibits vertical movement and the small-scale turbulence is confined into somewhat isolated patches that initially grow vertically and then collapse into ''pancakes vortices'' (e.g., see Fonseka et al. 1998); in a neutral PSL, the large-

Corresponding author address: Dr. Peter P. Sullivan, NCAR, P.O. Box 3000, Boulder, CO 80307-3000.
E-mail: pps@ncar.ucar.edu

scale shear predominates and the turbulence organizes itself into an intermittent pattern of turbulent spots and vortices, propagating through a larger-scale, near-laminar flow (e.g., see Lin et al. 1996); in an unstable PSL, convection sets in, and the vertical transport in the surface layer is dominated by intense, small-scale convective plumes (e.g., see Schmidt and Schumann 1989). Another modeling difficulty with the PSL is linked with the variability of the energy containing motions: spectral measurements in the atmospheric surface layer (e.g., see Kaimal et al. 1972) indicate that the velocity and temperature fluctuations exhibit a Kolmogorov spectrum with a peak frequency depending on the stability of the layer. At fixed height and mean horizontal velocity, there is a tendency for the peak to shift to higher frequencies as the layer becomes more stable. For the data presented in Kaimal et al. (1972), the peak of the vertical-velocity fluctuation is shifted toward higher frequencies by about one order of magnitude with respect to the peak frequency of horizontal velocities or temperature. These features make it difficult to use standard LES procedures, in which the filtering between large and small scales is done via a global, scale-independent method. Therefore, a successful approach to small-scale modeling must start from the basic equations and take into account both the integral-scale variability and small-scale intermittency, processes that so far have been given little attention in the subgrid-modeling community.

A natural way of dealing with intermittent flows is decomposition via localized wave packets. There are several mathematical transforms associated with this decomposition; two well-known examples are the Gabor and wavelet transforms. When decomposing a flow into wave packets, the dimensionality of the representation increases from $D + 1$ (D space, 1 time) to $2D + 1$ because both physical and spectral space coordinates are included. However, the information required to represent the flow need not increase because small-scale features are localized and fewer Gabor or wavelet modes are needed compared to a full Fourier representation. Also, by taking advantage of the locality of wavenumbers in a wavelet or Gabor representation, it is possible to implement a scale-dependent cutoff filter. And, in addition, small-scale features are enstrophic or palenstrophic and less energetic than the larger scales; hence, they couple most strongly to the large-scale dynamics, and their mutual nonlinear interaction may be neglected to first order. In other words, the dynamics of the small scales are primarily nonlocal in scale coordinates. This simplifies the dynamics of the small scales as they are linear in phase space, with conditions determined only by the large-scale flow. This simplification allows both analytic computations of the small-scale dynamics in terms of the large scales and a numerical algorithm that allows computation of the small-scale dynamics using a particle-in-cell method.

The first application of these modeling ideas was made for the β-plane model in geophysics by Dyachenko et al. (1992). It was then followed by an application to compressible flows by Nazarenko et al. (1995) and an application in 2D turbulence by Dubrulle and Nazarenko (1998), Nazarenko and Laval (1998), and Laval et al. (2000). The results were then generalized in Nazarenko et al. (1999), Nazarenko et al. (2000), and Dubrulle et al. (2001) for irrotational and pure shear flows. In particular, it was shown analytically that small-scale turbulence is responsible for the shear reduction in the large-scale flow, in agreement with experimental data. The formalism also allows for an exact analytic computation of the stationary mean shear profile in two dimensions. The resulting profile was shown to be either logarithmic, algebraic, or exponential, in agreement with a recent classification due to Oberlack (Oberlack 1999a,b). On the whole, this small-scale modeling approach is a significant improvement over conventional subgrid-scale models because it is derived directly from the basic equations. As such, it involves no adjustable parameters and can be generalized to other flows; for example, rotation and magnetic effects are easily included.

We should note that other subgrid models similar in spirit to the one described here have been proposed. Domaradzki and Saiki (1997), Katopodes et al. (2000), and Zhou et al. (2001) all attempt to model the subgrid-scale velocity as opposed to the subgrid-scale flux using various prescriptions. The attractive features of these models are that no (or minimal) closure constants are required and an eddy-viscosity assumption relating resolved and subgrid fields is not needed. Physical processes like energy backscatter can automatically be accommodated.

In the above studies, the prescription of the subgrid velocity is primarily confined to scales that are two times smaller than the grid mesh. Our proposed model differs in that the equations for the subgrid-scale velocity follow directly from the governing fluid mechanical equations, which then in principle apply at all scales below the mesh scale.

Our paper is outlined as follows; we first present the formalism involved in the derivation of our subgrid model in sections 2 and 3. These sections are rather technical but helpful for those interested in the details. The derivation of the subgrid model starting from the governing equations is given in section 4, and the major assumptions of the model are evaluated using numerical simulation databases in section 5. A summary is given in section 6.

2. Spatial filtering

a. Definition

We introduce a filter function $G(\mathbf{x})$ in order to separate the large and small scales of the flow. For reasons of convenience that will appear in section 3, we choose a separable filter function

$$G(\mathbf{x}) = \prod_i G_i(x_i), \tag{1}$$

where G_i are positive functions normalized to unity. Their support is concentrated over modes with characteristic length L_i. Thus

$$G_i(x_i) = \frac{1}{L_i}\tilde{G}_i\left(\frac{x_i}{L_i}\right), \tag{2}$$

where $\tilde{G}_i$ are functions which decay rapidly for large arguments. The choice of the characteristic scales L_i will be further discussed in section 4a. Using this filter, we decompose the velocity field into resolved (large-scale) and subgrid (small-scale) components:

$$\mathbf{u}(\mathbf{x}, t) = \mathbf{U}(\mathbf{x}, t) + \mathbf{u}'(\mathbf{x}, t),$$
$$\mathbf{U}(\mathbf{x}, t) \equiv \overline{u} = \int G(\mathbf{x} - \mathbf{x}')\mathbf{u}(\mathbf{x}', t)\, d\mathbf{x}'. \tag{3}$$

b. Properties

The scale filtering we have introduced is in the spirit of LES, where the large scales are simulated subject to a parameterization of the small scales. In the present case, the filter-scale separation is dictated by physical considerations (see section 4a). We note that the spatial-filtering and time-averaging operators do not always obey the same rules. For example, the filtering of the product of two filtered quantities is not necessarily the product of the filtered quantities; $\overline{\overline{u}\,\overline{v}} \neq \overline{u}\,\overline{v}$. This is because the beating of two small (intermediate) wavenumbers can generate a large wavenumber. Similarly, the filtering of a product of a small-scale quantity and a large-scale filtered quantity is not necessarily zero, since the beating of a large wavenumber and a small (intermediate) can produce an intermediate wavenumber. As we shall see, this difference produces additional terms in the averaged equations when compared to the standard Reynolds-stress decomposition based upon ensemble averaging underlying all second-order closure models of the PSL (Mellor and Yamada 1974; Mellor and Yamada 1982).

Another important difference between LES filtering and Reynolds averaging is the ability to commute derivative operators with spatial filters; for Reynolds averaging, derivatives and averaging commute, whereas for LES filtering, this is not the case in general. To see this, consider the filter of the quantity $\partial_1 u$ and integrate by parts over x_1'. We obtain:

$$\begin{aligned}\overline{\partial_1 u} &= \int G(\mathbf{x} - \mathbf{x}')\partial_{x_1'} u(\mathbf{x}')\, d\mathbf{x}' \\ &= \int dx_2\, dx_3 [G(\mathbf{x} - \mathbf{x}')u(\mathbf{x}')]_{x_1^{\min}}^{x_1^{\max}} \\ &\quad - \int [\partial_{x_1'} G(\mathbf{x} - \mathbf{x}')]u(\mathbf{x}')\, d\mathbf{x}'. \end{aligned} \tag{4}$$

By symmetry, the derivative with respect to x_1' in the second term of the rhs of (4) is the negative of the derivative with respect to x_1, which can then be taken out of the integral, giving a term $\partial_1 \overline{u}$. We then see that filtering and differentiation commute only provided the surface term (*the first term in the rhs*) is zero. If not, this term has to be taken into account in the derivation of the LES equations. When dealing with unbounded systems, this problem of commutivity is not important, for one usually considers physical quantities that tend to zero at infinity. Noncommutivity shows up when dealing with finite size systems (or variable computational meshes; e.g., Ghosal and Moin 1993), where boundary conditions may reflect some physical processes. In the PSL, this is the situation in the vertical direction. At the surface $z = 0$, we have to take into account the boundary conditions on the momentum and heat flux.

3. Gabor transform

a. Definition

Our ultimate goal is to derive an equation set for the small (subgrid) scales, as a function of the large (resolved) scales. However, we would like to take into account the strong intermittency of the small scales. We shall do this by decomposing the fields into wave packets using the Gabor transformation (Nazarenko et al. 1999)

$$\hat{u}'(\mathbf{x}, \mathbf{k}, t) = \int f(\mathbf{x} - \mathbf{x}')e^{i\mathbf{k}\cdot(\mathbf{x}-\mathbf{x}')}\mathbf{u}'(\mathbf{x}', t)\, d\mathbf{x}', \tag{5}$$

where $\mathbf{k}$ denotes the wavenumber vector. For reasons of convenience, which will appear later, we choose $f(\mathbf{x}) = [G(\mathbf{x})]^{1/2}$ (since the filter G is a positive function, this is always possible). We could also have achieved the same decomposition using a wavelet transformation (Arneodo et al. 1997), but Gabor transforms are more flexible in analytic computations.

b. Properties of the Gabor transform

The inverse Gabor transform is obtained by integration over $\mathbf{k}$:

$$f(0)\mathbf{u}'(\mathbf{x}, t) = \frac{1}{(2\pi)^2}\int \hat{\mathbf{u}}'(\mathbf{x}, \mathbf{k}, t)\, d\mathbf{k}. \tag{6}$$

The commutation of a Gabor transform and a partial derivative is subject to surface terms dependent on boundary conditions. The proof is analogous to that given in section 2b. Note, the derivative of the Gabor transform may be approximated by

$$\partial_i \hat{\mathbf{u}}' \approx ik_i\hat{\mathbf{u}}' + O[1/(L_* k)], \tag{7}$$

where L_* is the typical scale of the large-scale flow. Technically speaking, $\epsilon = 1/(kL_*)$ defines the cutoff scale between large and small scales, and ϵ is a parameter much less or less than one. Rigorous expansions in terms of ϵ are possible (Dubrulle and Nazarenko 1998;

Nazarenko et al. 1999; Nazarenko et al. 2000), but here we give a more heuristic derivation of the large- and small-scale equations.

Next consider the Gabor transform of a quantity involving the product of a function varying over large scales (e.g., $\mathbf{U}$) and a function varying over small scales (e.g., $\mathbf{u}'$):

$$\widehat{\mathbf{U}\mathbf{u}'} = \int f(\mathbf{x} - \mathbf{x}')e^{i\mathbf{k}\cdot(\mathbf{x}-\mathbf{x}')}\mathbf{U}(\mathbf{x}', t)\mathbf{u}'(\mathbf{x}', t)\, d\mathbf{x}'. \quad (8)$$

Because the kernel f varies over scales of order $1/k = \epsilon L_*$, while U varies over scales of order L_*, one can Taylor expand the function U around the point $\mathbf{x}'$ as a function of ϵ. To first order in ϵ, and after integration by parts, we then obtain:

$$\widehat{U_j\mathbf{u}}'(\mathbf{x}, \mathbf{k}, t) = U_j(\mathbf{x}, t)\hat{\mathbf{u}}' + i\nabla_i[U_j(\mathbf{x}, t)]\nabla_{k_i}\hat{\mathbf{u}}'. \quad (9)$$

This expansion will be used in developing the solution of the small-scale equations.

Finally, consider the filtered product of subgrid-subgrid quantities, that is, the subgrid stress $\overline{u_i' u_j'}$. Using our definition of filtering (3), $f^2 = G$, and the definition of the Dirac delta function $\delta(x' - x'') = (2\pi)^{-D} \int e^{ik(x-x')}e^{-ik(x-x'')}\, dk$, we can write the subgrid stress at point $\mathbf{x}$ and time t as a function of the Gabor transform:

$$\overline{u_i' u_j'} = \frac{1}{2(2\pi)^D} \int [\hat{u}_i'(\mathbf{k}, \mathbf{x}, t)\hat{u}_j'(-\mathbf{k}, \mathbf{x}, t) + \hat{u}_i'(-\mathbf{k}, \mathbf{x}, t)\hat{u}_j'(\mathbf{k}, \mathbf{x}, t)]\, d\mathbf{k}. \quad (10)$$

c. Local filtering

Being local in wavenumber space, the Gabor transform allows for a filtering procedure using a nonhomogeneous (i.e., spatially varying nonglobal) length scale. Indeed, the Fourier transform with respect to x of a Gabor mode $\hat{u}(k, x, t)$ is given by

$$FT(\hat{u})(k, q, t) = FT(G)(k + q)FT(u)(q). \quad (11)$$

Because G is a filter with support concentrated over scales of the order of $1/k_c$, we can approximate its Fourier transform by a step function

$$FT(G)(q) = \begin{cases} 1, & q < k_c, \\ 0, & q > k_c. \end{cases} \quad (12)$$

Consequently, the Fourier transform of $\hat{u}$ obeys:

$$FT(\hat{u}) = \begin{cases} FT(u)(q), & |k + q| < k_c, \\ 0, & |k + q| > k_c. \end{cases} \quad (13)$$

Using the Schwartz inequalities $\|k| - |q\| < |k + q| < |k| + |q|$, we see that for any Gabor mode such that $|k| > k_c + k_*$, where k_* is an arbitrary cutoff wavenumber that may depend on x, its Fourier transform has no component at $|q| < k_*$ [assuming (12) to be true]; that is, the Gabor mode is concentrated in scales smaller than $1/k_*(x)$. Therefore, by keeping those Gabor modes with an appropriately chosen wavenumber k, we can implement a local filtering procedure. Note also that the Gabor transform formalism allows anisotropic filtering with different conditions specified for each wavenumber component.

4. Derivation of the dynamical equations

a. Notation, approximations, and basic equations

The PSL is a nearly incompressible, stratified fluid layer. The Boussinesq approximation to the basic equations is

$$\begin{aligned} \partial_j u_j &= 0, \\ \partial_t u_i + \partial_j(u_i u_j) &= -\partial_i p - g_i\beta(\theta - T_0) + \nu\Delta u_i, \\ \partial_t\theta + \partial_j(u_j\theta) &= \kappa\Delta\theta, \end{aligned} \quad (14)$$

where $\mathbf{u}$ and θ are the velocity and potential temperature, T_0 is a reference temperature (e.g., just above the ground), p is the pressure (divided by constant density), $\mathbf{g} = (0, 0, -g)$ is the gravitational vector, β is the coefficient of thermal expansion, and ν and κ are the kinematic viscosity and thermal diffusivity.

To derive the large- and small-scale equations from the basic equations, we shall use a filtering procedure in which the filtering scales are chosen so that large-scale motions are much more energetic than the small-scale motions. This will guarantee that the dominant interactions at small scales are between large (resolved) scales and small (subgrid) scales. This will enable a linearization of the small-scale dynamics, and, therefore, analytic solutions. In Part II of this paper (Dubrulle et al. 2002), we derive the equation following a traditional filtering procedure, keeping in mind the possibility of performing local filtering via properly selected Gabor modes to take into account the variation of the integral scale as one gets closer to the ground. The technical difficulties involved in this case will be addressed in a future work devoted to the numerical implementation of our model.

b. Resolved-scale equations

Equations for the resolved scales of motion are obtained by application of the spatial filter (3) to the individual terms of the basic equations (14). Taking into account the noncommutivity between the filter and the z component of the Laplacian for the horizontal velocity and the temperature (see section 2), at the resolved level we obtain

$$\partial_j U_j = 0,$$

$$\partial_t U_i + \partial_j \overline{U_i U_j} + \partial_j \overline{U_i u_j + U_j u_i} + \partial_j \overline{u_i u_j} = -\partial_i P - g_i \beta(\Theta - T_0) + \nu \Delta U_i + \mathcal{S}_i^{(u)},$$
$$\partial_t \Theta + \partial_j \overline{U_j \Theta} + \partial_j \overline{u_j \Theta + U_j \theta} + \partial_j \overline{u_j \theta} = \kappa \Delta \Theta + \mathcal{S}^{(\theta)}. \quad (15)$$

In these equations, we have dropped primes on subgrid components for simplicity; this means that from now on, resolved quantities are denoted by uppercase letters, while subgrid-scale quantities are denoted by lowercase letters. We have also introduced two surface terms

$$\mathcal{S}_i^{(u)} = -u_*^2 G_3(z)\delta_{i3}, \qquad \mathcal{S}^{(\theta)} = Q_0 G_3(z). \quad (16)$$

Here, the surface momentum and heat flux are given by $\nu \partial_z U(z = 0) = -u_*^2$ and $\kappa \partial_z \Theta(z = 0) = Q_0$. Note that the surface terms depend explicitly on the filter choice and on the cutoff scale in the vertical direction; however, they are only important at a distance from the surface, which is less than the vertical cutoff scale as the G_3 function vanishes for scales larger than the cutoff scale.

Note that the large-scale motions depend on the small-scale motions through two subgrid stress terms; the subgrid–subgrid product $\overline{u_i u_j}$, and the resolved–subgrid cross term $\overline{U_i u_j + U_j u_i}$. Traditional subgrid modeling usually parameterizes these two terms together, via assumptions about the velocity correlations. However, recent measurements in the PSL by Tong et al. (1999) indicate that these two kinds of subgrid stresses contribute differently to the total subgrid stress, which cannot be captured by a single, global parameterization. Here, we adopt an alternative approach and focus on modeling efforts on the subgrid-scale dynamics using a direct estimate of the subgrid-scale velocities instead of the subgrid-stress components. This enables us to treat resolved–subgrid and subgrid–subgrid terms independently. The estimate of the subgrid velocity is obtained by a parameter-free procedure, using a dynamical equation derived directly from the basic equations.

c. A nonlocal subgrid-scale model

Consider the subgrid component of the basic equations (14):

$$\partial_j u_j = 0,$$
$$\partial_t u_i + \partial_j[(U_i + u_i)(U_j + u_j) - \overline{(U_i + u_i)(U_j + u_j)}] = -\partial_i p - g_i \beta \theta + \nu \Delta u_i - \mathcal{S}_i^{(u)},$$
$$\partial_t \theta + \partial_j[(U_j + u_j)(\Theta + \theta) - \overline{(U_j + u_j)(\Theta + \theta)}] = \kappa \Delta \theta - \mathcal{S}^{(\theta)}. \quad (17)$$

Subgrid motions are generated through two types of processes: the nonlinear cascade mechanism and surface forcing. Several terms contribute to the nonlinear interaction; their orders of magnitude will likely differ.

Assuming nonlinear subgrid–subgrid interactions to be negligible; i.e., $u_i u_j - \overline{u_i u_j} \ll U_i u_j - \overline{U_i u_j}$ and $\theta u_j - \overline{\theta u_j} \ll \Theta u_j - \overline{\Theta u_j}$, the subgrid model equations become

$$\partial_j u_j = 0,$$
$$\partial_t u_j + U_j \partial_j u_i = -\partial_i p - g_i \beta \theta - u_j \partial_j U_i + \nu \Delta u_i + F_i^{(u)},$$
$$\partial_t \theta + U_j \partial_j \theta = -u_j \partial_j \Theta + \kappa \Delta \theta + F^{(\theta)}, \quad (18)$$

where the forces $F^{(u)}$ and $F^{(\theta)}$ are given by

$$F_i^{(u)} = -\mathcal{S}_i^{(u)} + \partial_j(\overline{U_i U_j} - U_i U_j) + \partial_j \overline{U_j u_i} + \partial_j \overline{U_i u_j},$$
$$F^{(\theta)} = -\mathcal{S}_i^{(\theta)} + \partial_j(\overline{U_j \Theta} - U_j \Theta) + \partial_j \overline{U_j \theta} + \partial_j \overline{u_j \Theta}. \quad (19)$$

Note that $F_i^{(u)}$ and $F^{(\theta)}$ depend on both the surface terms, and on filtered resolved–subgrid interactions. We call $F_i^{(u)}$ and $F^{(\theta)}$ pseudoforces because of their dependence on the subgrid scales; i.e., they are not purely ''external.'' In Part II, $F_i^{(u)}$ and $F^{(\theta)}$ will be replaced with truly externally prescribed forces in order to obtain analytic solutions for mean velocity and temperature profiles, and for vertical fluctuations.

The equations describing the dynamics of the subgrid scales, although superficially complicated, have a simple structure; they are *linear*, inhomogeneous equations for the subgrid motions, with the forcing occurring via the nonlinear cascade among the resolved–subgrid scales. As we mentioned in section 1, the linear feature is the essential simplification that makes it possible to obtain estimates of the subgrid velocities by a semi-Lagrangian type of procedure involving only resolved timescales. This leads to a computational cost comparable to typical LES (Laval et al. 2000; Laval et al. 2001). Also, the linear structure of the equations enables analytic solutions of the subgrid-scale dynamics in terms of large-scale quantities. Substitution of the small-scale solution into the large-scale equation results in a closed system for the large scales from which we can obtain analytic solutions for the mean velocity and temperature profiles (see Part II).

All these advantages of the small-scale equations can be realized by a decomposition of the subgrid scales over spatially localized (Gabor) modes, optimized to describe small-scale intermittency. We thus take the Gabor transform of (18) and use (9). To leading order in the scale separation parameter ϵ, we obtain the system

$$\partial_j \hat{u}_j = 0,$$
$$\partial_t \hat{u}_i + U_j \partial_j \hat{u}_i - \partial_j(U_m k_m)\partial_{k_j} \hat{u}_i = -ik_i \hat{p} - \hat{u}_j \partial_j U_j - g_i \beta \hat{\theta} - \nu \mathbf{k}^2 \hat{u}_i + \hat{F}_i^{(u)}$$
$$\partial_t \hat{\theta} + U_j \partial_j \hat{\theta} - \partial_j(U_m k_m)\partial_{k_j} \hat{\theta} = -\hat{u}_j \partial_j \Theta - \kappa \mathbf{k}^2 \hat{\theta} + \hat{F}^{(\theta)}, \quad (20)$$

where $\mathbf{k} = (k, q)$ is the wavenumber. Note that no new surface terms arise here because the subgrid quantities have necessarily zero boundary conditions. The set of

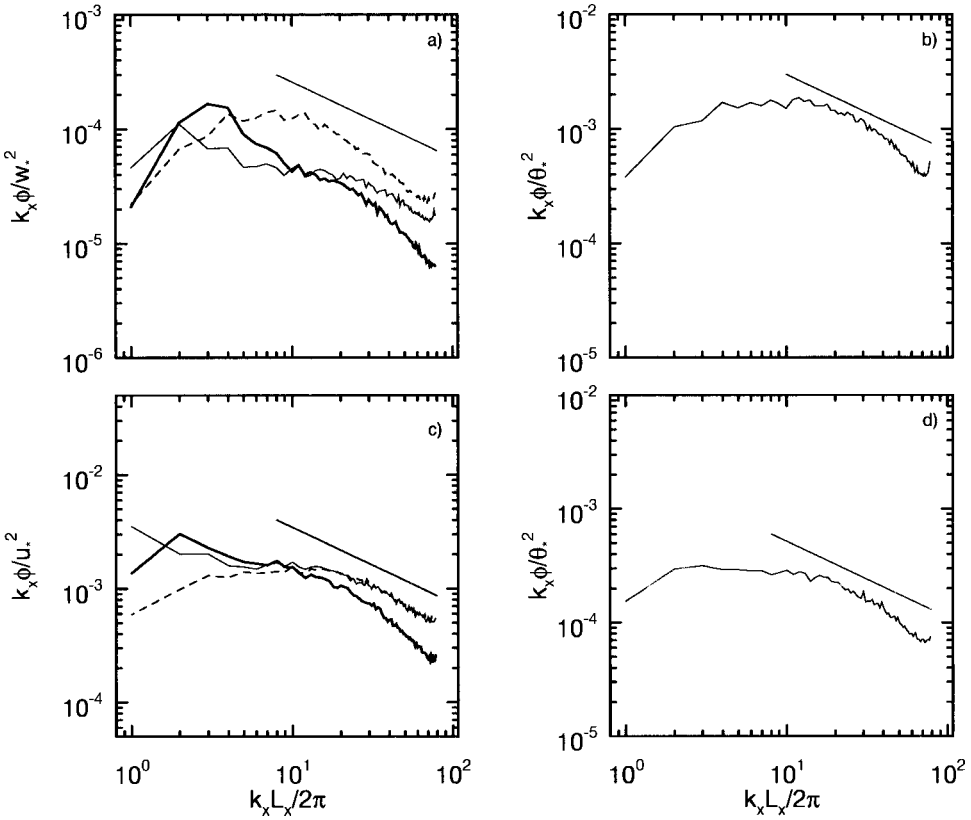

FIG. 1. One-dimensional velocity and temperature spectra $\phi(k_x)$ from 240^3 LES at $z/z_i = 0.1$: (a) and (b) velocity and temperature spectra for free-convection case, (c) and (d) shear-buoyancy case. The (heavy-solid, light-solid, dashed) lines in (a) and (c) are spectra of the velocities (u, v, w). Velocity spectra are normalized by w_*^2 and u_*^2 for the free-convection and shear-buoyancy cases, respectively. The thin straight lines depict inertial range scaling for unfiltered data.

equations (20) are next put into a set of ray equations by introducing the total derivative:

$$D_t \equiv \partial_t + U_j\partial_j - \partial_j(U_ik_i)\partial_{k_j}, \tag{21}$$

which is a total time derivative in phase space ($\mathbf{x}$, $\mathbf{k}$, t) provided $\mathbf{k}$ and $\mathbf{x}$ satisfy

$$D_tx_i = U_i, \qquad D_tk_i = -k_j\partial_iU_j. \tag{22}$$

These ray equations describe the motion of wavepackets, whose center moves at the large-scale velocity, and whose wavenumber varies according to the local shear, thereby describing the transfer of energy between large and small scales. Next, using the incompressibility constraint to eliminate the pressure, the system (20) is rewritten as

$$\begin{aligned} D_t\hat{u}_i &= \left(\frac{2k_ik_m}{\mathbf{k}^2} - \delta_{im}\right)\hat{u}_j\partial_jU_m + \left(\frac{k_ik_j}{\mathbf{k}^2} - \delta_{ij}\right)g_j\beta\hat{\theta} \\ &\quad - \nu\mathbf{k}^2\hat{u}_i + F_i^{(\hat{u})^\perp}, \\ D_t\hat{\theta} &= -\hat{u}_j\partial_j\Theta - \kappa\mathbf{k}^2\hat{\theta} + \hat{F}^{(\theta)}, \end{aligned} \tag{23}$$

TABLE 1. Simulation parameters and solution properties.

Run	Free convection	Shear buoyancy
Domain size (L_x, L_y, L_z) (km)	(5, 5, 2)	(3, 3, 1)
Grid spacing (Δx, Δy, Δz) (m)	(20.8, 20.8, 8.3)	(12.5, 12.5, 4.2)
PBL height z_i (m)	1000	500
Monin–Obukhov L (m)	<-1460	-34.4
$-z_i/L$	<1.40	14.5
Surface heat flux Q_* (K m s^{-1})	0.06	0.06
Friction velocity u_* (m s^{-1})	<0.08	0.30
Convective velocity w_* (m s^{-1})	1.26	1.0
Geostrophic wind U_g (m s^{-1})	0.0	5.0
Mean wind at $z/z_i = 0.1$ (m s^{-1})	$\approx$0.0	3.9

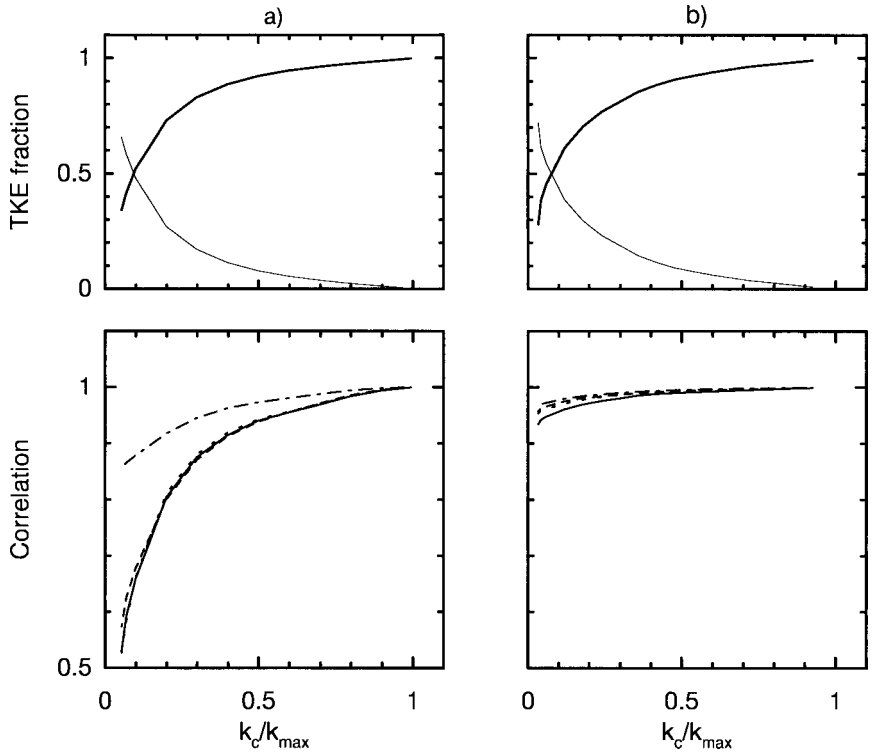

FIG. 2. Correlation of complete small-scale advection term with the contributions from the resolved–resolved and resolved–subgrid interactions for the small-scale velocity components and temperature using 240^3 LES. Here u is the solid line, v the dotted line, w the dash–dotted line, and θ the dashed line; (a) free-convection case and (b) shear-buoyancy case. (upper panels) The fraction of turbulent kinetic energy (relative to the total) in the resolved (heavy line) and small-scale (thin line) fields.

where $F^{(u)^\perp}$ is the divergence-free component of the force:

$$F_i^{(u)^\perp} = \left(\delta_{ij} - \frac{k_i k_j}{\mathbf{k}^2}\right) F_j^{(u)}. \tag{24}$$

The equation set (15) and (23), where the subgrid stresses are computed using (10), constitute the main equations of our flow model. The subgrid model is dynamical because it allows for temporal and spatial evolution of the subgrid stress. It has been derived directly from the basic equations of the PSL and allows many natural generalizations.

5. A priori tests of the nonlocal hypothesis

Presently, extensive 3D observational datasets of the flow fields in the PSL are not available to test the nonlocal scaling hypothesis. The emphasis of most field campaigns is on deducing fluxes and variances from single-point time series, information which is insufficient to estimate spatially filtered variables [the measurements of Tong et al. (1999) are a noteable exception, see also Meneveau and Katz (2000)]. New experimental methods are required to measure velocity, pressure, and temperature in multiple dimensions at sufficient spatial resolution to estimate the magnitude of all terms in (17).

In the absence of field observations, we will use LES of the planetary boundary layer (PBL) and direct numerical simulation (DNS) of a stably stratified shear layer as databases for evaluation of our nonlocal scaling hypothesis. Laval et al. (1999) has already employed such an approach but those numerical simulations were of 2D flows. We are aware that both LES and DNS are imperfect surrogates for real turbulence in the PSL; LES becomes questionable near the surface because of poor resolution and subgrid-scale (SGS) influences, and DNS is limited by low Reynolds number. However, we attempt to minimize these shortcomings by using high-resolution LES and the largest Reynolds number DNS available.

Our a priori tests follow standard procedures. The 3D data is first filtered in 2D horizontal (x–y) planes using a sharp (Fourier) cutoff filter at varying nondimensional cutoff wavenumber k_c. No explicit filtering is applied in the vertical direction because of the uncertainty of defining a filter function in the presence of a solid boundary. The resolved fields then contain all motions

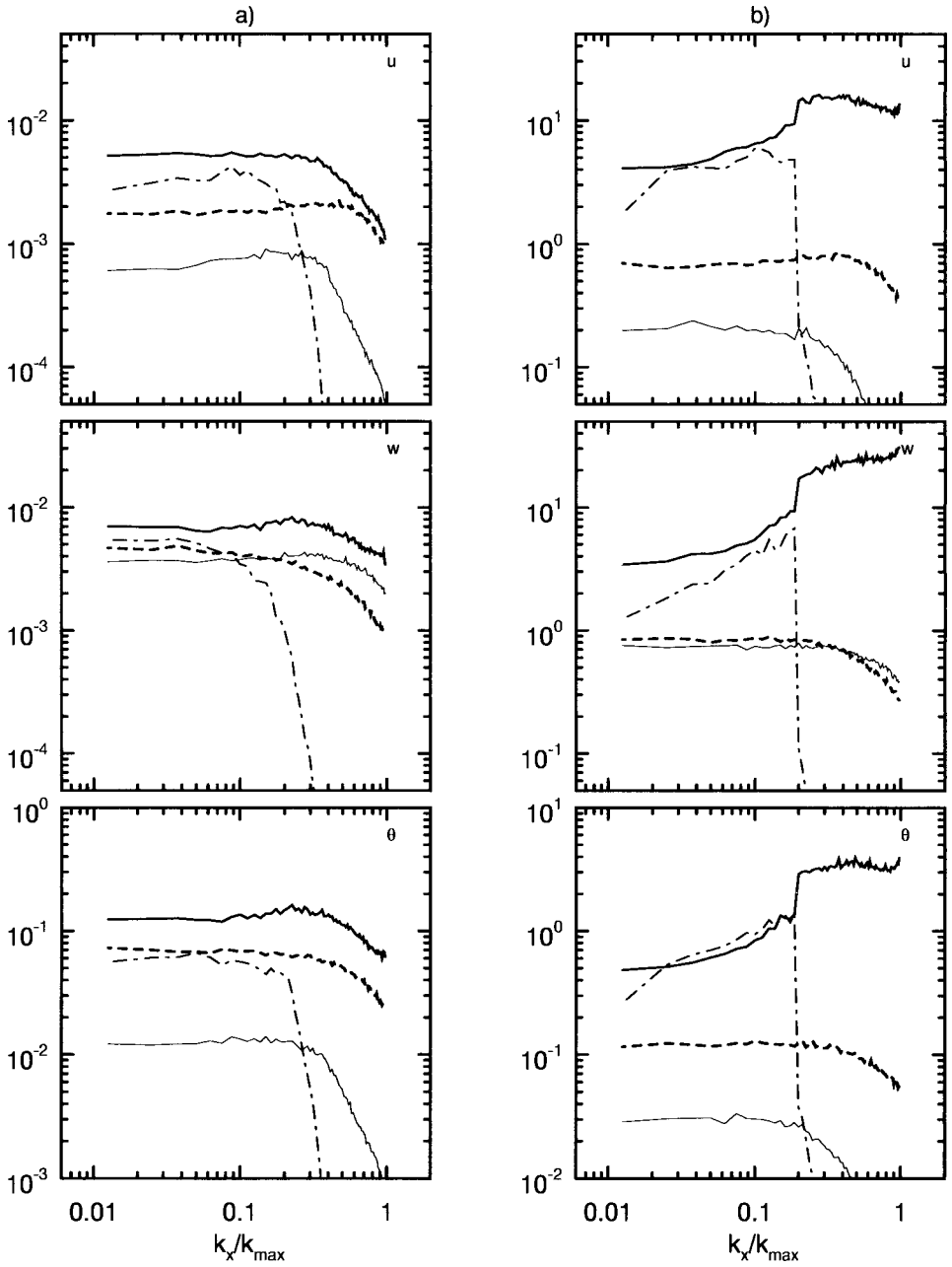

FIG. 3. Spectral content of the interaction terms in the small-scale advection equations: (a) free-convection case with $k_c/k_{max} = 0.2$ and (b) shear-buoyancy case with $k_c/k_{max} = 0.2$. Various curves are heavy-solid line advection of small scales by resolved scales (*b* term), thin-solid line advection of resolved scales by small scales (*c* term), dash–dot line advection of resolved scales by resolved scales (*a* term), and dashed line advection of small scales by small scales (*d* term). The vertical axis in each plot is a normalized squared Fourier coefficient.

with $(k_x, k_y)^1 < k_c$, while the subgrid fields are composed of wavenumbers $|\mathbf{k}| > k_c$. The exact quantitative relationships between resolved and subgrid fields are filter dependent; however, we expect the qualitative relationships between resolved and subgrid quantities to be filter-independent based on the results of Laval et al. (1999). The critical aspect of our a priori testing focuses on estimating the magnitude of the resolved–resolved, resolved–subgrid, and subgrid–subgrid interactions in the small-scale equations. In order to estimate the contribution of these various interaction terms to the evo-

[1] Here (k_x, k_y) are horizontal wavenumbers in the (x, y) directions, respectively.

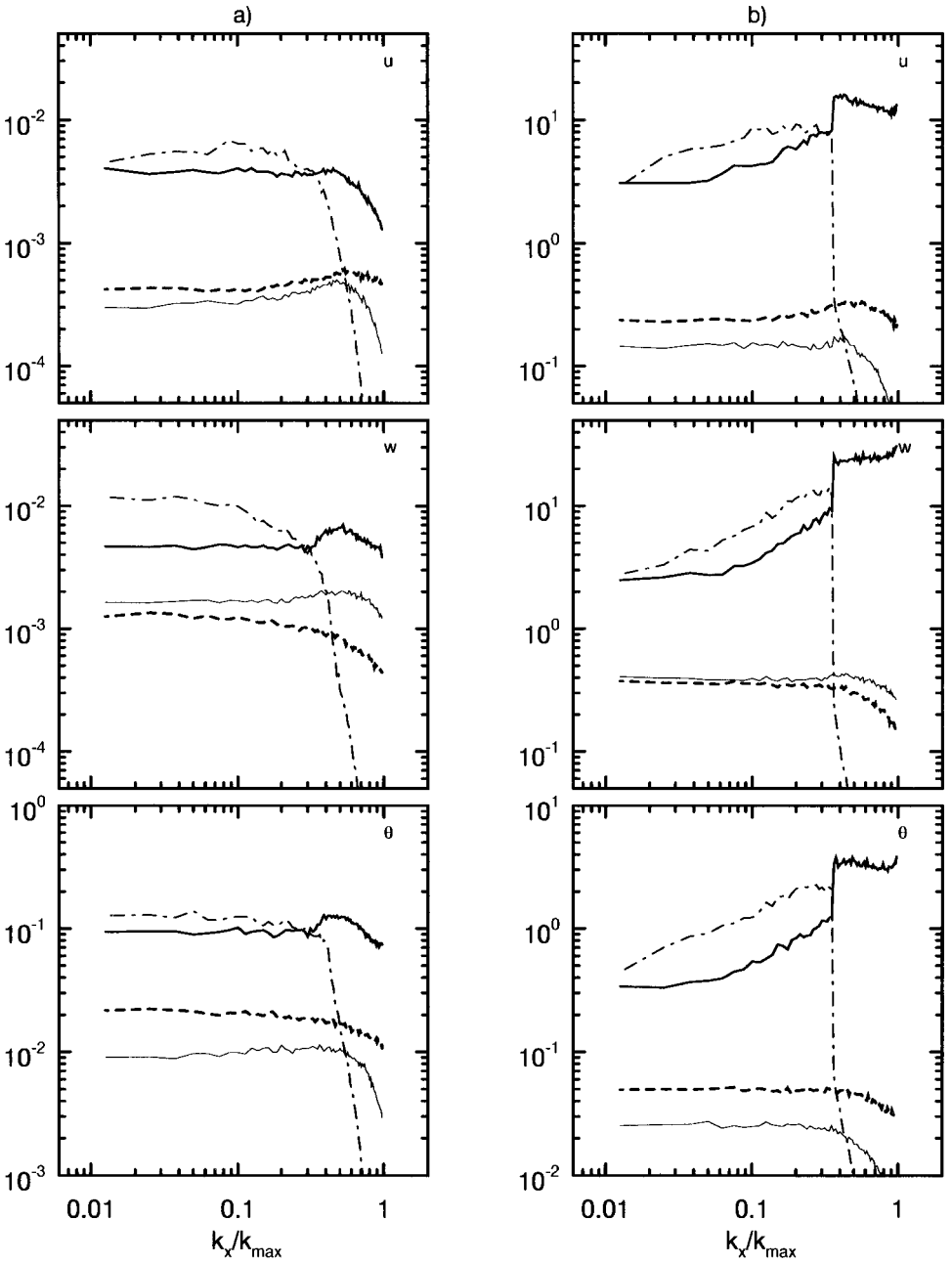

FIG. 4. Spectral content of the interaction terms in the small-scale advection equations: (a) free-convection case with $k_c/k_{max} = 0.4$ and (b) shear-buoyancy case with $k_c/k_{max} = 0.36$. Labeling is the same as in Fig. 3.

lution of the subgrid velocity fields, a statistical analysis of the small-scale advection term was carried out. For convenience, in (17) let

$$A_i^{(\mathrm{vel})} = \frac{\partial}{\partial x_j}[(U_i + u_i)(U_j + u_j) - \overline{(U_i + u_i)(U_j + u_j)}] = [a_i + b_i + c_i + d_i - \overline{(a_i + b_i + c_i + d_i)}]^{\mathrm{vel}}, \tag{25}$$

where

$$a_i^{(\mathrm{vel})} = \frac{\partial_i(U_i U_j)}{\partial x_j}, \qquad b_i^{(\mathrm{vel})} = \frac{\partial(u_i U_j)}{\partial x_j},$$
$$c_i^{(\mathrm{vel})} = \frac{\partial(U_i u_j)}{\partial x_j}, \qquad d_i^{(\mathrm{vel})} = \frac{\partial(u_i u_j)}{\partial x_j}. \tag{26}$$

Physically, the resolved–resolved component $a_i^{(\mathrm{vel})}$ embodies transport of large-scale eddies by large eddies, the resolved–subgrid interactions $b_i^{(\mathrm{vel})}$, $c_i^{(\mathrm{vel})}$ represent transport of small-scale eddies by large eddies and large eddies

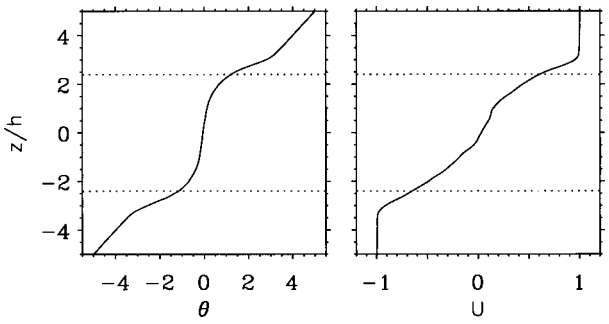

FIG. 5. Vertical profiles of average nondimensional velocity and temperature for stably stratified shear (Kelvin–Helmholtz) flow. The dotted lines indicate the ''edge'' region of the turbulent layer.

by small ones, and the subgrid–subgrid term $d_i^{(\mathrm{vel})}$ denotes transport of small eddies by small eddies. We note that (25) can be expressed in standard notation as

$$A_i^{(\mathrm{vel})} = -\frac{\partial}{\partial x_j}(L_{ij} + \overline{C_{ij}} - C_{ij} + \overline{R_{ij}} - R_{ij}), \quad (27)$$

where $L_{ij} = \overline{U_iU_j} - U_iU_j$ is the Leonard term, $C_{ij} = u_iU_j + u_jU_i$ is the unfiltered cross term, and $R_{ij} = u_iu_j$ is the unfiltered subgrid–subgrid term. However, alternate definitions of L_{ij}, C_{ij}, and R_{ij} are possible (see Germano 1986). In a similar fashion, the advective term in the small-scale temperature equation can be written as

$$A^{(\mathrm{temp})} = \frac{\partial}{\partial x_j}[(U_j + u_j)(\Theta + \theta) - \overline{(U_j + u_j)(\Theta + \theta)}]$$
$$= [a + b + c + d - \overline{(a + b + c + d)}]^{(\mathrm{temp})}, \quad (28)$$

where

$$a^{(\mathrm{temp})} = \frac{\partial(\Theta U_j)}{\partial x_j}, \qquad b^{(\mathrm{temp})} = \frac{\partial(\theta U_j)}{\partial x_j},$$
$$c^{(\mathrm{temp})} = \frac{\partial(\Theta u_j)}{\partial x_j}, \qquad d^{(\mathrm{temp})} = \frac{\partial(\theta u_j)}{\partial x_j}. \quad (29)$$

a. LES results

LES of the PBL was carried out using the code and simulation procedures described in Sullivan et al. (1996) with an SGS model specifically designed to capture Monin–Obukhov profiles in the surface layer (Sullivan et al. 1994) using 240^3 gridpoint calcula-

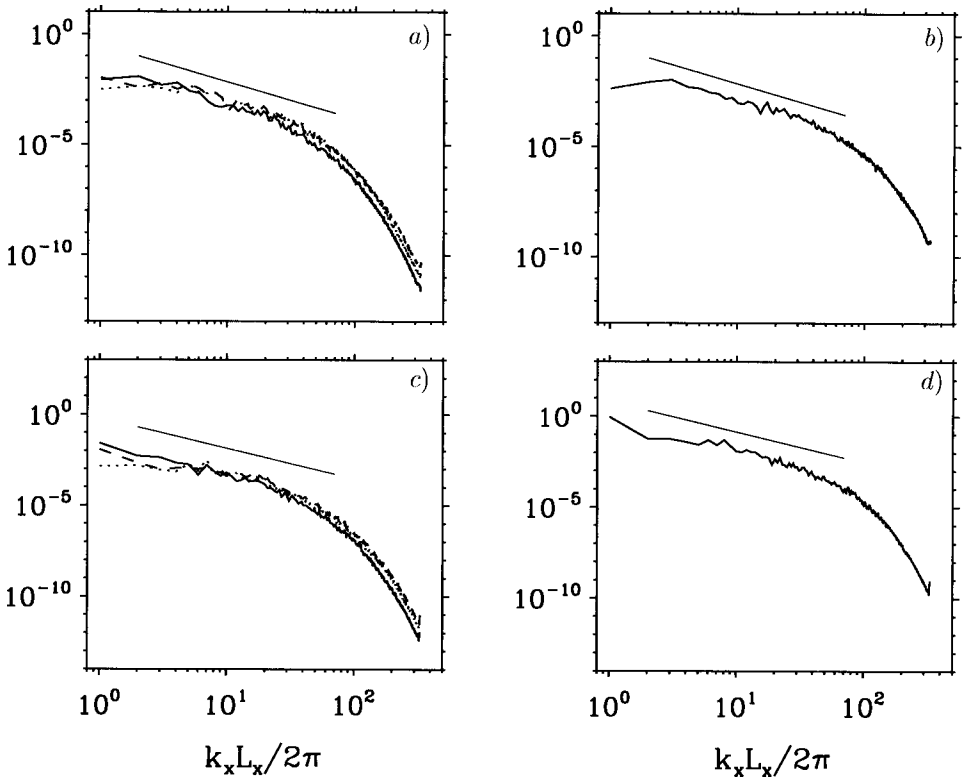

FIG. 6. One-dimensional streamwise velocity and temperature spectra $\phi(k_x)$ from $1000 \times 360 \times 2000$ mode DNS: (a) and (b) velocity and temperature spectra at midlayer $z/h = 0$; (c) and (d) at edge layer $z/h = 2.4$. The (solid, dashed, dotted) lines in (a) and (c) are spectra of the velocities (u, v, w), respectively. The thin straight lines depict inertial range scaling ($k^{-5/3}$) for unfiltered data.

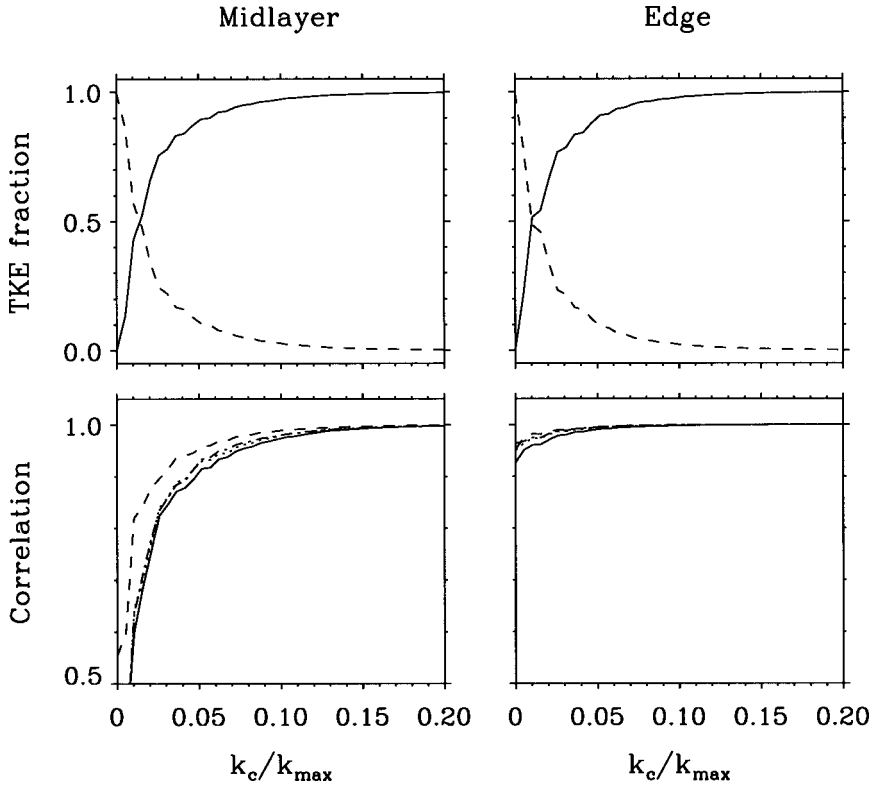

FIG. 7. Correlation of complete small-scale advection term with the contributions from the resolved–resolved and resolved–subgrid interactions for the small-scale velocity components and temperature from stably stratified DNS. Here u is the solid line, v the dash–dot line, w the long-dashed line, and θ the dotted line. (upper panels) The fraction of TKE (relative to the total) in the resolved (heavy line) and small-scale (dashed line) fields.

tions.[2] Two cases were simulated, a ''free convection'' (no mean wind) case and a ''shear-buoyancy'' (combined shear and buoyancy forcing) case (see also Moeng and Sullivan 1994). Several 3D volumes were archived from each simulation after 2 h of simulation time (about 5000 time steps). For our purposes, x–y slices of data were examined in detail at the vertical location $z/z_i = 0.1$ [here z_i denotes the average PBL height based on the maximum local gradient; see Sullivan et al. (1998)]. At this location, which is just at the upper boundary of the PSL, the SGS turbulent kinetic energy (TKE) is less than 10% of the total TKE and the SGS heat flux is less than 2% of the total heat flux. Thus, the SGS influences are expected to be small. Further details of the simulations are reported in Table 1. In Fig. 1, one-dimensional power spectra of the velocity components and temperature are shown for both cases. Reasonable agreement with inertial-range scaling is observed. We should note that these results have not been corrected for the implicit filtering associated with finite differencing in the vertical direction (e.g., see Schmidt and Schumann 1989) and the integration of a finite number of Fourier modes to compute the spectra (see Moeng and Wyngaard 1988). Both effects cause departures from inertial-range scaling at high wavenumbers. Overall the shape of the spectra in the free-convection case are in good agreement with those of Schmidt and Schumann (1989).

The relative importance of the nonlinear small-scale interaction terms can be gauged from the correlation of the advective terms with and without the subgrid–subgrid contribution. A normalized correlation coefficient

$$\rho = \frac{\langle A(A - d + \overline{d})\rangle}{(\langle A^2\rangle)^{1/2}[\langle (A - d + \overline{d})^2\rangle]^{1/2}}, \qquad (30)$$

was computed for each of the three velocity components and temperature. The angle brackets operator denotes an average over an x–y plane. The correlations are shown in Fig. 2 as a function of the nondimensional cutoff wavenumber k_c/k_{max}[3] for the free-con-

[2] A new version of the LES code was recently ported to the IBM SP2 using the message passing interface (MPI), allowing the increased number of gridpoints reported here.

[3] Here $k_{max} = 2\pi/3\Delta x$ is the maximum wavenumber accounting for dealiasing with the 2/3 rule.

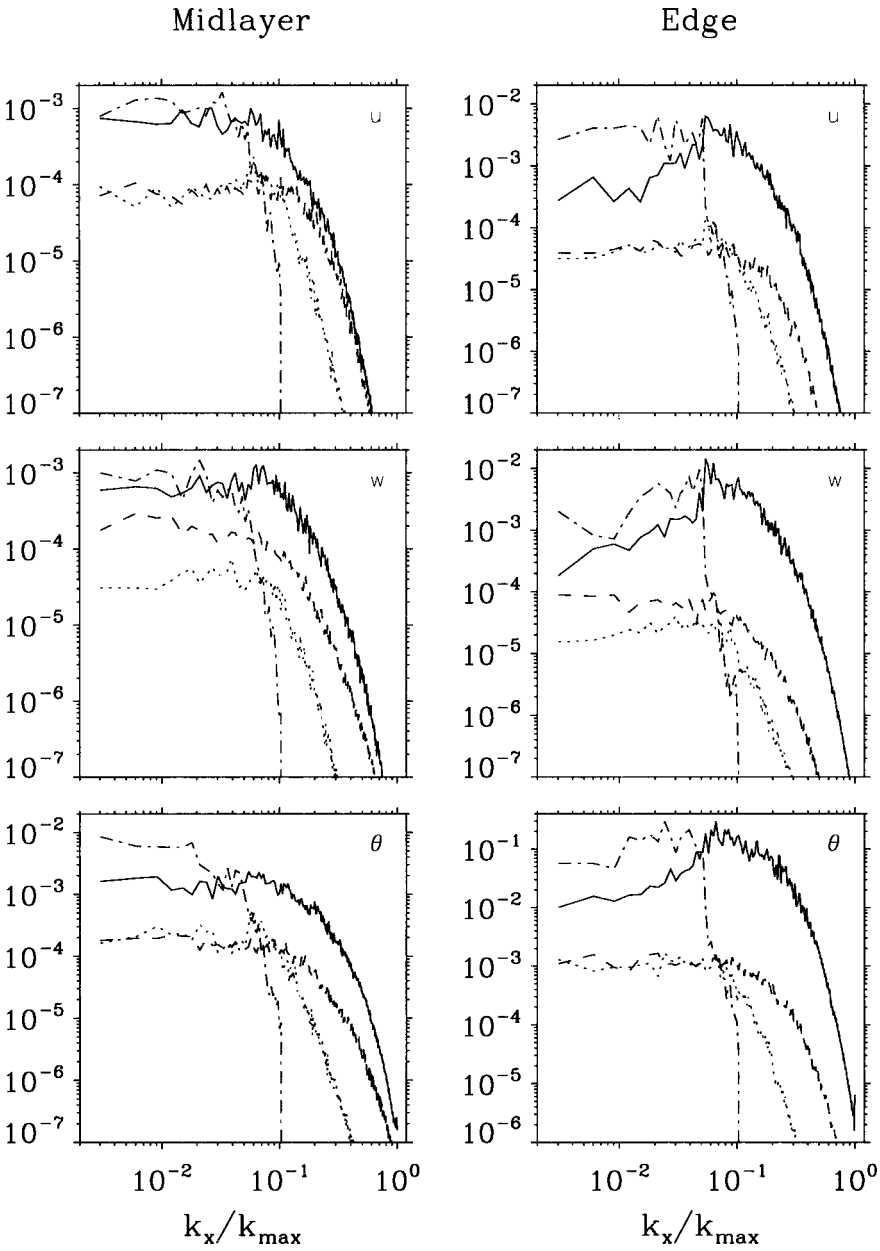

FIG. 8. Spectral content of the interaction terms in the small-scale advection equations for stably stratified shear flow with $k_c/k_{max} = 0.052$: (left) midlayer ($z/h = 0$) and (right) edge layer ($z/h = 2.4$). Various curves are solid line advection of small scales by resolved scales (*b* term), long-dashed line advection of resolved scales by small scales (*c* term), dash–dot line advection of resolved scales by resolved scales (*a* term), and dashed line advection of small scales by small scales (*d* term). The vertical axis in each plot is a normalized squared Fourier coefficient.

vection and shear-buoyancy cases. The first impression of these results is that the subgrid–subgrid interaction term in the small-scale equations [i.e., the *d* term in (25) and (28)] is subdominant to the resolved–resolved and resolved–subgrid terms based on the good correlation for all variables for both cases considered. Closer inspection of the results shows that the correlation coefficients are always larger than 0.5 over the entire range of k_c considered. Note that a reasonable level of correlation is maintained even at $k_c/k_{max} < 0.1$ when the fraction of TKE in the small scales is greater than 50% of the total TKE. A striking feature of the variations is the very high correlation (greater than 0.95) in the shear-buoyancy case compared to the free-convection case over all cutoff wavenumbers. Since the surface heating is identical in our two simulations, the high correlations in the shear-buoyancy case results from the presence of a mean

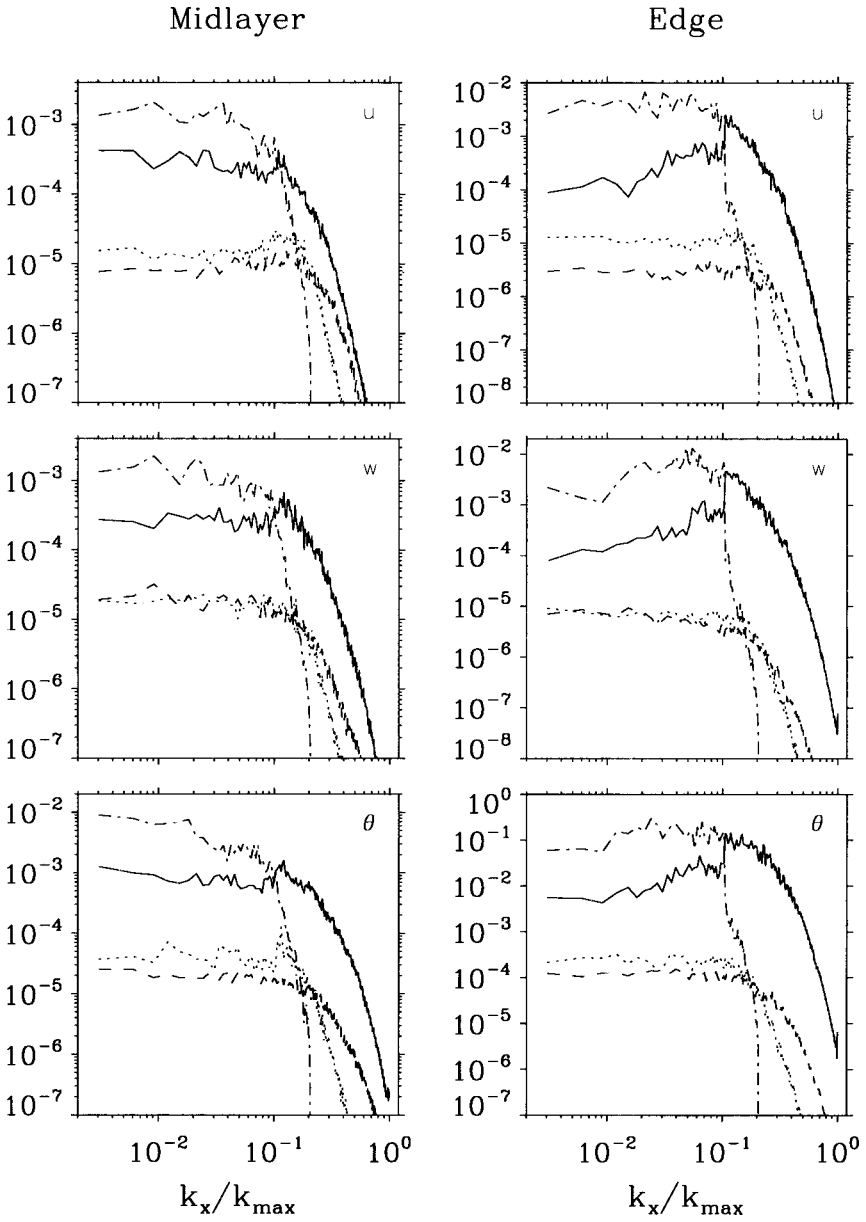

FIG. 9. Spectral content of the interaction terms in the small-scale advection equations for DNS with $k_c/k_{max} = 0.103$: (left) midlayer at $z/h = 0$ and (right) edge layer at $z/h = 2.4$. Labeling is the same as in Fig. 8.

wind shear. The (u, v, θ) correlations in the free-convection case reach levels comparable to the shear-buoyancy case (greater than 0.9) when $k_c/k_{max} > 0.4$. Note that in the free-convection case, the w correlation clearly exceeds the (u, v, θ) correlations; a similar but weaker trend is also apparent in the DNS results (see Fig. 7). In the LES simulations, the spectral content of the w field is shifted toward higher wavenumbers compared to the u field (see Fig. 1a), which might be a possible source of the differences in the magnitude of the correlations shown in Fig. 2. Overall, the good correlations obtained in the free-convection and shear-buoyancy cases support our nonlocal hypothesis; that is, that the small-scale dynamics are significantly determined by their interaction with the larger scales.

Next, in order to dig further into the details of the small-scale advection, spectra of the various interaction terms are considered. Specifically, we computed 1D spectra of the terms (a_i, b_i, c_i, d_i), i.e., of the divergence of the resolved–resolved, resolved–subgrid, and subgrid–subgrid interactions. In this respect, we are following the analysis of 2D flow fields presented by Laval et al. (1999). The results are dis-

played in Figs. 3 and 4 for two values of cutoff wavenumber $k_c/k_{\max}$ for the free-convection and shear-buoyancy cases.

First, we notice that the relative balance between the interaction terms is dependent on k, k_c, and the flow simulated. For instance, the resolved–resolved interaction is large for $k < k_c$ and small for $k > k_c$, for both simulations, while the magnitude of the resolved–subgrid interaction term b increases for $k > k_c$ in the shear-buoyancy case but is either constant or decreases slightly in the free-convection case. The crucial common feature in all of these results is the subdominance of the subgrid–subgrid interaction; that is, term d is at most the second largest contributor to the small-scale transport. Detailed inspection of the results also helps explain the high correlation in the shear-buoyancy flow. Transport of small eddies by the resolved large-scale motions (which contain a mean wind) is clearly dominant, about one order of magnitude larger than the subgrid–subgrid term. This is not entirely surprising since term b is also the dominant term in Taylor's hypothesis, which is often adopted as an approximation for weak turbulence (e.g., Hinze 1975, p. 47). However, our term b includes all the resolved scales (not just the mean wind) as the advective velocity for the small scales. Also, as k_c increases the resolved–resolved interaction term becomes an increasingly important player, further supporting our scaling argument. These same trends also hold true in the free-convection case but to a lesser extent because of the absence of a mean wind shear.

It is further interesting to notice that the spectral content of the small-scale w transport possesses some unique features compared to the (u, v, θ) advection, especially apparent in the free-convection case. The transport of large scales by small scales (term c) exceeds the subgrid–subgrid interaction only in the small-scale w equation. In fact, the contribution of the c term helps lead to the increased correlation observed in Fig. 2a at low cutoff wavenumbers. Based on these results, one might expect to use different modeling for small-scale u and w near a solid surface. For example, one may want to introduce an anisotropic turbulent eddy viscosity in the equation for w to account for the action of the local interactions (see Laval et al. 2001; Laval et al. 2001, Langevin models of turbulence: DSTA, RNG or ROT?, submitted to *Phys. Fluids*) for tests and discussion of this procedure in 3D homogeneous turbulence). Overall, the small-scale advection is a complex, scale, and flow-dependent process. However the above results support our hypothesis that the small-scale dynamics are primarily determined by the larger scales. We have found that these results are insensitive to grid resolution using $500^2 \times 100$ simulations.

b. DNS results

Turbulence in the PSL is frequently stably stratified because of the diurnal cycle of solar forcing. Compared to the unstable or neutral case, the stable PBL is characterized by intermittent, small-scale, weak turbulence (e.g., Mahrt 1998). To examine the influences of stable stratification for our nonlocal scale hypothesis, we utilize the DNS databases generated by Werne and Fritts (1999) and Werne and Fritts (2000) of a 3D stably stratified Kelvin–Helmholtz (KH) instability in the absence of any bounding surfaces.[4] In this transient flow, turbulence is initiated by 3D perturbations on the background shear profile $u = U_o \tanh(z/h)$ under constant (i.e., z independent), stable stratification. Here U_o and h are constant velocity and length scales and z is the vertical coordinate. DNS were performed at the highest Reynolds number to date, $\mathrm{Re} = U_o h/\nu = 2500$, at a Richardson number, $R_i = 0.05$; at this R_i the shear layer is dynamically unstable. The layer Reynolds number $\mathrm{Re}_L = \Delta U \Delta L/\nu$, based on the final depth of and the velocity difference across the resulting turbulent layer (ΔL and ΔU, respectively) reached $\mathrm{Re}_L \approx 30\,000$ during the evolution of the flow. The simulations utilize $1000 \times 360 \times 2000$ spectral modes. A description of the computational procedures and details of the turbulence statistics are available in Werne and Fritts (1999) and Werne and Fritts (2000).

Our analysis of the DNS database follows the same procedures as for the LES (see section 5). We chose a single 3D volume at a nondimensional time where 3D turbulence is fully developed. Vertical profiles of the horizontally averaged nondimensional temperature and velocity at this time are shown in Fig. 5. Based on the shape of these profiles we further focus our attention on the planes at midlayer $z/h = 0$ in the core of the mixed layer and at the layer edge $z/h = \pm 2.4$ for detailed analysis. These planes were selected since they cover a range of conditions; at midlayer the turbulence is continuous and the mean horizontal velocity is $\langle u \rangle = 0$, while at the layer edge the turbulence (and hence the entraining process) is intermittent and $\langle u \rangle$ is significant. Note that over the entire vertical extent the mean temperature gradient, $\partial_z \langle \theta \rangle$, is positive (i.e., the stratification is stable). The scale content of the turbulence is depicted in Fig. 6. An inertial subrange ($k^{-5/3}$ variation) is observed for all flow variables at both the midlayer and edge-layer locations.

The correlation of the advective terms with and without the subgrid–subgrid contribution [see Eq. (30)] for a range of cutoff wavenumbers is presented in Fig. 7. Similar to the LES, high correlation is obtained (coefficients greater than 0.5) for almost all cutoff wavenumbers despite the presence of stable stratification. For example, at $z/h = 0$ the correlations

[4] We realize that this flow is only an approximate model for the surface layer of the planetary boundary layer, which is strongly influenced by the ground. However, the KH flow contains stable stratification, which is the important physical process we wish to include in our analysis.

are at least 0.8 where the TKE fraction in the subgrid field is 30% of the total. Note that the correlations are greatest in the edge region, where turbulence is intermittent and the entrainment process strongly depends on the stratification. Despite the complexity of the dynamics in this region, the mean horizontal flow dominates, and as a result, the correlations behave like those for the LES shear-buoyancy case. The variation of the correlations at midlayer, however, differ notably and instead behave like those obtained in our LES free-convection case. This is because the mean wind vanishes at midlayer, and turbulent mixing has restratified the mean density profile to near neutrality (see Fig. 5).

In Figs. 8 and 9 spectral decompositions of the various interaction terms in the small-scale advection [see Eqs. (26) and (29)] are shown for the midlayer and edge-layer for cutoff wavenumbers $k_c/k_{\max} =$ (0.052, 0.103). The important feature to notice in these plots is that even in the presence of stable stratification the resolved–subgrid interaction (term *b*) is dominant compared to the subgrid–subgrid interaction (term *d*) over almost the entire wavenumber range for all flow variables. Similar to the a priori test with LES, this dominance increases as the cutoff wavenumber shifts to the right and as the mean advective velocity increases. The impact of the large-scale advective velocity is readily apparent in the edge region; e.g., in the *w*-equation term *b* is almost two orders of magnitude larger than term *d* in the wavenumber range $k_x/k_{\max} > 0.1$. The closest approach of the subgrid–subgrid and resolved–subgrid interaction terms occurs at very high wavenumbers in the midlayer for the *u* equation. A similar, but weaker, tendency is also found in our LES free-convection simulation (see upper-left panel of Fig. 3). At present, the physical process at work is unknown, but we note that at these high wavenumbers viscous effects are clearly important influences in the DNS. Results from 2D simulations utilizing hyperviscosity (Laval et al. 1999) did not show such an effect.

Overall our a priori tests using numerical databases support our nonlocal-scale hypothesis for 3D flows with unstable, neutral, and stable stratification.

6. Summary

In this paper, we have developed a new model for the atmospheric surface layer that involves no adjustable parameters. This model involves the coupling of two dynamical equations; one for the large (resolved) scales of motion and another for the small (subgrid) scale velocity. The equations are coupled through resolved–resolved and resolved–subgrid interactions. The subgrid-scale equation is a linear inhomogeneous equation, where the forcing occurs via the kinetic and potential energy cascade from resolved to subgrid scale. It is derived from the basic equations of motion under the assumption of nonlocality of the interactions at small scales. This assumption is tested using data from numerical simulations (both LES and DNS) for flows with varying stratification. In the companion paper, we use this new model to predict the variation of the integral scale of the vertical motions, the mean temperature and velocity profiles, and the variance of temperature and vertical velocity in the atmospheric surface layer. Our results show that our model, derived from the basic equations via a physical approximation, has the correct symmetry and asymptotic requirements built in, which is not necessarily the case for traditional subgrid modeling. The next step is to implement a full numerical model (resolved plus subgrid equations), in order to see whether quantitative agreement can be reached via the consistent computation of the constants appearing in our analytic solutions. This is the subject of an ongoing work, which will be reported in future publications.

Acknowledgments. We thank Eun-Jin Kim for interesting discussions. John Wyngaard pointed out an inconsistency in a previous version of the manuscript. BD was partially funded by a NATO fellowship, PPS was supported under the ONR CBLAST Initiative N00014-00-C-0180, and JW is partially supported by AFOSR F49620-98-C-0029, DOE DE-FG03-99ER62839, NSF ATM-9708633, and NASA NASW-99026. DNS calculations were conducted on the 512-PE Cray T3E at ERDC, with additional resources at PSC and NCSA. NCAR is sponsored by the National Science Foundation.

REFERENCES

Arneodo, A., J.-F. Muzy, and S. Roux, 1997: Experimental analysis of self-similarity and random processes: Application to fully developed turbulence data. *J. Phys. II France,* **7,** 363–370.

Domaradzki, J. A., and E. M. Saiki, 1997: A subgrid scale model based on the estimation of unresolved scales of turbulence. *Phys. Fluids,* **9,** 2148.

Dubrulle, B., and S. Nazarenko, 1998: Interaction of turbulence and large scale vortices in 2D incompressible fluids. *Physica D,* **110,** 123–138.

——, J.-P. Laval, S. Nazarenko, and N. Kevlahan, 2001: Derivation of mean equilibrium profiles in plane parallel geometry using a new dynamical subgrid model. *Phys. Fluids,* **13,** 2045–2064.

——, ——, and P. P. Sullivan, 2002: A new dynamical subgrid model for the planetary surface layer. Part II: Analytical computation of fluxes, mean profiles, and variances. *J. Atmos. Sci.,* **59,** 877–891.

Dyachenko, A. I., S. Nazarenko, and V. E. Zakharov, 1992: Wave-vortex dynamics in drift and beta plane turbulence. *Phys. Lett. A,* **165,** 330–333.

Fonseka, S. V., H. J. S. Fernando, and G. J. F. van Heijst, 1998: Evolution of an isolated turbulent region in a stratified fluid. *J. Geophys. Res.,* **103,** 24 857–24 868.

Germano, M., 1986: A proposal for a redefinition of the turbulent stresses in the filtered Navier–Stokes equations. *Phys. Fluids,* **29,** 2323–2324.

Ghosal, S., and P. Moin, 1993: The basic equations for the large

eddy simulation of turbulent flows in complex geometry. *J. Fluid Mech.,* **282,** 1–27.
Hinze, J. O., 1975: *Turbulence.* McGraw-Hill, 790 pp.
Kaimal, J. C., J. C. Wyngaard, Y. Izumi, and O. R. Coté, 1972: Spectral characteristics of surface-layer turbulence. *Quart. J. Roy. Meteor. Soc.,* **98,** 563–589.
Katopodes, F. V., R. L. Street, and J. H. Ferziger, 2000: A theory for the subfilter-scale model in large-eddy simulation. Stanford University Environmental Fluid Mechanics Laboratory Tech. Rep. 2000-K1.
Lavalle, J.-P., B. Dubrulle, and S. Nazarenko, 1999: Nonlocality of interaction of scales in the dynamics of 2D incompressible fluids. *Phys. Rev. Lett.,* **83,** 4061–4064.
——, ——, and ——, 2000: Dynamical modeling of subgrid scales in 2D turbulence. *Physica D,* **142,** 231–253.
——, ——, and ——, 2001: Nonlocality and intermittency in 3D turbulence. *Phys. Fluids,* **13,** 1995–2012.
Lin, C.-L., J. C. McWilliams, C.-H. Moeng, and P. P. Sullivan, 1996: Coherent structures and dynamics in a neutrally stratified planetary boundary layer flow. *Phys. Fluids,* **8,** 2626–2639.
Mahrt, L., 1998: Stratified atmospheric boundary layers and breakdown of models. *Theor. Comp. Fluid Dyn.,* **11,** 263–280.
Mellor, G. L., 1973: Analytical prediction of the properties of the stratified planetary surface layers. *J. Atmos. Sci.,* **30,** 1061–1069.
——, and T. Yamada, 1974: A hierarchy of turbulent closure models for planetary boundary layers. *J. Atmos. Sci.,* **30,** 1791–1806.
——, and ——, 1982: Development of a turbulent closure model for geophysical fluid problems. *Rev. Geophys. Space Phys.,* **20,** 851–875.
Meneveau, C., and J. Katz, 2000: Scale-invariance and turbulence models for large-eddy simulation. *Annu. Rev. Fluid Mech.,* **32,** 1–32.
Moeng, C.-H., and J. C. Wyngaard, 1988: Spectral analysis of large-eddy simulations of the convective boundary layer. *J. Atmos. Sci.,* **45,** 3573–3587.
——, and P. P. Sullivan, 1994: A comparison of shear and buoyancy driven planetary-boundary-layer flows. *J. Atmos. Sci.,* **51,** 999–1022.
Nazarenko, S., and J.-P. Laval, 1998: Non-local two-dimensional turbulence and Batchelor's regime for passive scalars. *J. Fluid Mech.,* **408,** 301–321.
——, N. J. Zabusky, and T. Scheidegger, 1995: Non linear sound–vortex interactions in an inviscid isentropic fluid: A two fluid model. *Phys. Fluids,* **7,** 2407–2419.
——, N. Kevlahan, and B. Dubrulle, 1999: Nonlinear theory for rapid distortion of inhomogeneous turbulence. *J. Fluid Mech.,* **390,** 325–336.
——, ——, and ——, 2000: Nonlinear RDT theory of near wall turbulence. *Physica D,* **138,** 158–176.
Oberlack, M., 1999a: Symmetries, invariance and scaling-laws in inhomogeneous turbulent shear flows. *Flow, Turb. Combustion,* **62,** 111–135.
——, 1999b: Similarity in non-rotating and rotating turbulent pipe flows. *J. Fluid Mech.,* **379,** 1–22.
Schmidt, H., and U. Schumann, 1989: Coherent structure of the convective boundary layer derived from large-eddy simulations. *J. Fluid Mech.,* **200,** 511–562.
Sullivan, P. P., J. C. McWilliams, and C.-H. Moeng, 1994: A subgrid-scale model for large-eddy simulation of planetary boundary-layer flows. *Bound.-Layer Meteor.,* **71,** 247–276.
——, ——, and ——, 1996: A grid nesting method for large-eddy simulation of planetary boundary-layer flows. *Bound.-Layer Meteor.,* **80,** 167–202.
——, C.-H. Moeng, B. Stevens, D. H. Lenschow, and S. D. Mayor, 1998: Structure of the entrainment zone capping the convective atmospheric boundary layer. *J. Atmos. Sci.,* **55,** 3042–3064.
Tong, C., J. C. Wyngaard, and J. G. Brasseur, 1999: Experimental study of the subgrid-scale stresses in the atmospheric surface layer. *J. Atmos. Sci.,* **56,** 2277–2292.
Werne, J., and D. C. Fritts, 1999: Stratified shear turbulence: Evolution and statistics. *Geophys. Res. Lett.,* **26,** 439–442.
——, and ——, 2000: Structure functions in stratified shear turbulence. *10th HPC User Group Conf.,* Albuquerque, NM, U.S. Department of Defence, 1–11.
Wyngaard, J. C., 1992: Atmospheric turbulence. *Annu. Rev. Fluid Mech.,* **24,** 205–233.
Zhou, Y., J. G. Brasseur, and A. Juneja, 2001: A resolvable subfilter-scale model specific to large-eddy simulation of underresolved turbulence. *Phys. Fluids,* **13,** 2601–2610.